Multi-sensor magnetoencephalography with atomic magnetometers

Multi-sensor magnetoencephalography with atomic magnetometers

Cort N Johnson[1]**, P D D Schwindt**[1] **and M Weisend**[2]

[1] Sandia National Laboratories, PO Box 5800, Albuquerque, NM 87185-1082, USA
[2] Wright State Research Institute, 4035 Colonel Glenn Highway, Beavercreek, OH 45431, USA

E-mail: cort.johnson@alum.mit.edu and pschwin@sandia.gov

Abstract

The authors have detected magnetic fields from the human brain with two independent, simultaneously operating rubidium spin-exchange-relaxation-free magnetometers. Evoked responses from auditory stimulation were recorded from multiple subjects with two multi-channel magnetometers located on opposite sides of the head. Signal processing techniques enabled by multi-channel measurements were used to improve signal quality. This is the first demonstration of multi-sensor atomic magnetometer magnetoencephalography and provides a framework for developing a non-cryogenic, whole-head magnetoencephalography array for source localization.

(Some figures may appear in colour only in the online journal)

1. Introduction

Detecting the extremely weak magnetic fields produced by human biology requires highly sensitive magnetic detectors. For the past several decades, scientific and clinical advances in biomagnetism have been achieved predominantly using superconducting quantum interference device (SQUID) magnetometers and gradiometers (Sternickel and Braginski 2006). Prominent applications include magnetocardiography (MCG) (Koch 2004) and magnetoencephalography (MEG) (Hämäläinen *et al* 1993). While SQUID sensitivity, which can be as low as a few fT/$\sqrt{\text{Hz}}$ (1 fT = 10^{-15} T), adequately addresses the technical needs of biomagnetic detection, the cryogenic infrastructure required to operate SQUID-based systems is costly and inflexible. For example, SQUID-based MEG systems cannot accommodate a wide range of head sizes because their sensor geometry is necessarily fixed within a liquid helium dewar. Furthermore, the cost of the liquid helium required to keep SQUID-based systems at superconducting temperatures limits their installation to only well-funded organizations, and even with adequate funding the helium supplies are uncertain and inadequate supplies interrupt service. In contrast, atomic magnetometers (AMs) are near-room-temperature devices with suitable sensitivity and bandwidth for biomagnetic applications. As such, AMs have the potential to drastically reduce costs and enable reconfigurable arrays to accommodate head size, thereby extending the utility of MEG.

Over the past decade, AM technology has advanced into the sub-fT sensitivity range (Kominis *et al* 2003) with a record sensitivity of <0.2 fT/$\sqrt{\text{Hz}}$ (Dang *et al* 2010). As a result, arrays of AMs have been recognized as a strong candidate to replace SQUID technology in biomagnetic applications (Vrba *et al* 2006). Furthermore, techniques developed to solve the magnetic inverse problem using SQUID technology are compatible with proposed AM systems (Lima *et al* 2006). AMs measure magnetic fields by manipulating and interrogating the magnetic properties of alkali atomic vapours. Typically, the vapour is optically pumped into a collective magnetically-sensitive state and the resulting field-dependent optical properties are probed. Atomic density is adjusted to maximize sensitivity by controlling the vapour-cell temperature, with a typical operating range between room temperature and 200 °C, so in contrast with SQUIDs no cryogenics are required. The most sensitive AMs operate in a high-density, low-field regime where spin-exchange (SE) collisions do not interrupt the coherent interaction between the collective magnetic moment and the magnetic field (Allred *et al* 2002). While these spin-exchange-relaxation-free (SERF) magnetometers obtain unparalleled sensitivity, other styles of laser-based pump/probe configurations in addition to SERF have been used in biomagnetic recordings over the past decade.

Because MCG signals are roughly 1000 times larger than MEG signals (10^5 fT versus 10^2 fT), AMs designed for MCG do not need to approach the sub-fT regime. This allows for considerable flexibility in the pump–probe arrangement employed in AMs used for MCG and the dc field at which the magnetometer operates. The earliest recordings were performed in the 1980s with discharge-lamp optically pumped magnetometers (Livanov *et al* 1981, Fomin *et al* 1983). Laser-pumped AMs for MCG of several varieties have been constructed over the past decade. Caesium optical/radio-frequency double-resonance devices used in the phase-locked M_x mode have been used to generate spatial maps of the field produced by a beating heart (Bison *et al* 2003a, 2003b) and have been arrayed into a 19-channel second-order gradiometer imaging system (Bison *et al* 2009). MCG recordings have been performed in an unshielded environment with a device that probed a caesium coherent-population-trapping resonance (Belfi *et al* 2007). A chip-scale AM (CSAM) operating in the SERF regime has been developed that measures the modulation of pump beam intensity after passing through a microfabricated rubidium vapour cell. MCG recordings with the CSAM have been cross-validated with SQUID recordings (Knappe *et al* 2010). A four-channel modular array of rubidium SERF AMs that measure the Faraday rotation of a probe beam due to an external field has successfully detected not only adult (Wyllie *et al* 2012a) but also foetal (Wyllie *et al* 2012b) MCG signals.

Only SERF AMs have sufficient sensitivity to reliably detect MEG signals. The earliest AM MEG recordings were performed using large vapour cells and free-space laser beams (Xia *et al* 2006). SQUID-based MEG systems have a helmet-shaped array of sensors surrounding the head in order to perform spatial localization of neural sources, and an AM-based MEG system must also incorporate a helmet-style geometry. This is impossible with large vapour cells and free-space beams, so fibre-coupled SERF AM sensors have been developed that could potentially be arrayed around the head for whole-head MEG. These AMs are based upon either Faraday rotation of a linearly polarized probe beam (Johnson *et al* 2010) or absorption of a circularly polarized pump beam in a CSAM (Sander *et al* 2012). The Faraday rotation sensor has the advantages of gradiometric output and higher sensitivity while the CSAM volume is two orders of magnitude smaller, allowing its sensing volume to be much closer to the neural sources and enabling higher bandwidth. Both sensors have successfully detected MEG signals. In the present work, we extend our previous single-sensor AM MEG work (Johnson *et al* 2010) and take a significant step toward an AM MEG array for spatially-resolved brain imaging by measuring MEG signals simultaneously from two fibre-coupled, four-channel

AMs located on opposite sides of the head of a human subject. Using multi-channel signal processing techniques, we are able to significantly increase the MEG signal-to-noise ratio.

We will first present an overview of the relevant physics and the AM hardware design in section 2. In section 3, we will discuss our methods for recording MEG signals from adult human subjects, followed by a presentation of two-sensor (eight-channel) MEG data in section 4. Finally, we will conclude and discuss the prospects for developing large-scale AM arrays for MEG in section 5.

2. Atomic magnetometer physics and design

The general theory of operation of SERF magnetometers has been detailed previously (Allred *et al* 2002, Ledbetter *et al* 2008), and the specific implementation used in our sensor has also been discussed in considerable depth (Johnson and Schwindt 2010, Johnson *et al* 2010). We refer the reader to these resources for a more detailed exposition of SERF physics and will provide only a brief descriptive overview sufficient to understand the results presented in later sections.

2.1. Atomic magnetometer physics

AMs sense magnetic fields by establishing an average electron spin polarization $\mathbf{P} = \langle \mathbf{S} \rangle / S$ in an atomic vapour and detecting the resulting field-dependent changes in optical properties. The typical arrangement uses a sealed glass container with a small amount of an alkali species such as caesium, potassium, or rubidium deposited on the inner surface. Alternatively, silicon microfabrication techniques can be used to produce highly miniaturized (1–2 mm^3) vapour cells (Schwindt *et al* 2004). The atomic vapour density is determined by the temperature of the vapour cell, and heating the vapour cell is common to increase the density of atoms contributing to the magnetic signal.

A nonzero value for $\mathbf{P}$ is created by the optical pumping process (Happer and Mathur 1967) wherein the angular momentum of an optical field is transferred to the atomic sample. Most SERF implementations optically pump the vapour by passing a circularly polarized laser beam through the vapour cell. When the laser is tuned near a strong electronic transition from the ground state, $\mathbf{P}$ becomes oriented along the direction of beam propagation. In the presence of a magnetic field $\mathbf{B}$, $\mathbf{P}$ precesses around $\mathbf{B}$ according to $\dot{\mathbf{P}} = (\gamma/Q)\mathbf{P} \times \mathbf{B}$, where Q is the nuclear slowdown factor and $\gamma = g_s \mu_B / \hbar$ is the electronic gyromagnetic ratio with $g_s \approx 2$ and μ_B being the Bohr magneton. In addition to the free precession, several other processes impact the dynamics of $\mathbf{P}$ (Ledbetter *et al* 2008). Absorption of optical pumping photons resets the polarization along the beam direction, while collisions with vapour cell walls or other atoms serve to randomize the direction of the atomic magnetic moment. The rates of these processes add together to yield an overall decoherence rate Γ.

AMs can only reach the sub-fT sensitivity range (Kominis *et al* 2003, Dang *et al* 2010) by minimizing the sources of decoherence. The effects of wall collisions are minimized by either coating the vapour cell walls with specialized materials that preserve coherence during wall collisions (Balabas *et al* 2010) or by filling the vapour cell with an inert buffer gas that the alkali atoms must diffuse through in order to reach the walls. Effects from the dominant atomic collision decoherence mechanism, SE collisions, are eliminated entirely by operating in the low-field, high-density SERF regime. Under these conditions the SE collision rate is much higher than the magnetic precession frequency, and the coherence of the magnetic precession is preserved (Happer and Tang 1973, Happer and Tam 1977).

Consider an alkali vapour that is optically pumped at a rate R by a circularly polarized beam oriented along the z axis with magnetic field equal to zero in the x and z directions. The steady-state polarizations P_x and P_z as a function of the field B_y are given by (Ledbetter *et al* 2008)

$$P_x = -P_0 \frac{B_y \Delta B}{B_y^2 + \Delta B^2}, \tag{1}$$

$$P_z = P_0 \frac{\Delta B^2}{B_y^2 + \Delta B^2}, \tag{2}$$

where $P_0 = R/\Gamma$ is the ratio of the optical pumping rate to the decoherence rate and $\Delta B = \Gamma/\gamma$. The steady-state polarizations described in (1) and (2) can be converted to observable magnetometer signals in a few ways. First, the absorption of the circularly polarized pump beam depends on the value of P_z, resulting in an absorption spectrum that has an approximately Lorentzian lineshape as a function of B_y. A linear magnetometer signal can be obtained by modulating B_y and performing phase-sensitive detection of the measured absorption signal. Second, a linearly polarized probe beam oriented in the x (z) direction will have its plane of polarization rotated by an angle that is proportional to $P_x(P_z)$. Therefore, polarization analysis of the probe beam measures the field-dependent magnetic polarization of the gas. With the probe oriented along the x axis, (1) indicates a linear dependence on B_y in the portion of the dispersive Lorentzian curve near $B_y = 0$. A z-oriented probe beam probes the Lorentzian P_z lineshape, but a linear response to B_y can be generated by modulating B_y and performing phase-sensitive detection on the output of the polarization analyser. Alternatively, a signal linear in B_x can generated simply by zeroing B_y and modulating the field in the x direction rather than the y direction. Therefore, a z-oriented probe beam has the advantage of being able to measure either B_x or B_y by simply modulating the field in the direction of desired sensitivity.

2.2. Atomic magnetometer design

Our AM MEG sensors utilize a unique two-colour, single-optical-axis SERF design to pump and probe a ^{87}Rb vapour. Figure 1 shows a photograph of the hardware along with a schematic of its operation. The vapour cell is electrically heated to $\sim$150 °C with a resistive heater driven at 20 kHz, which is well above the $\sim$1–100 Hz frequency band relevant for MEG recordings (Hämäläinen *et al* 1993). The cell has a buffer gas of $\sim$8 × 10^4 Pa of helium to limit decoherence due to wall collisions and $\sim$4 × 10^3 Pa of nitrogen to prevent radiation trapping. A circularly polarized 795 nm laser tuned near the D1 line performs optical pumping, while Faraday rotation of a 780 nm probe laser near the D2 line is measured via polarimetry. The pump and probe light are delivered via the same polarization-maintaining optical fibre. A multi-order waveplate at the output of the fibre circularly polarizes the 795 nm light while maintaining linear polarization of the 780 nm light. The beam expands in free space to a diameter of $\sim$1 cm before being collimated. The collimated beam double-passes the cell via a retroreflecting mirror, and the 795 nm pump light is removed with a 780 nm bandpass filter prior to entering a polarization analyser consisting of a polarizing beamsplitter and two quadrant photodiodes. Using quadrant photodiodes in each arm of the analyser allows for the extraction of the magnetometer signal from each quadrant of the vapour cell, resulting in four magnetometer output channels acquired from the vapour cell housed in each sensor. Measurement of magnetic field gradients are possible by appropriate addition and subtraction of signals. The sensor is enclosed in a G10 fibreglass-epoxy composite vacuum vessel to limit
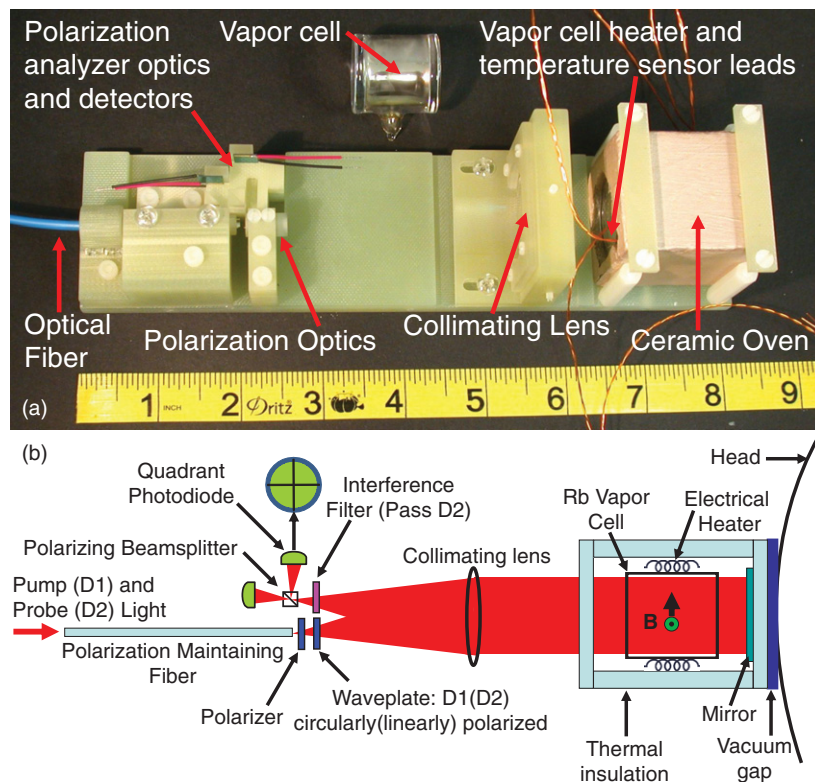
Figure 1. Sensor photograph (a) and schematic (b). Pump and probe light are delivered via a polarization-maintaining fibre. Polarization optics circularly polarize the pump and linearly polarize the probe. Both beams pass through the vapour cell, retroreflect, and pass back through the vapour cell before being focused onto a polarization analyser consisting of a polarizing beamsplitter and two quadrant photodiodes. The distance from the centre of the vapour cell to the scalp is ∼3 cm. (Figure modified and reprinted with permission from Johnson *et al* (2010). Copyright 2010 American Institute of Physics.)

thermal conduction between the heated vapour cell and the surface of the subject's head during MEG measurements.

The two-colour overlapped pump/probe scheme is advantageous because it allows for a simple, compact design and independent pump/probe parameter adjustment. Because the pump and probe beams propagate along a single axis, P_z is probed by the Faraday rotation measurement (see (2)). As a result, we must impose a modulated field in order to extract a linear magnetometer output. The orientation of the modulated magnetic field selects the sensitive axis of the device, so the sensor can be configured to measure either B_x or B_y by modulating the field in the x or y directions respectively. Phase-sensitive detection is accomplished by demodulating the output of the polarimetry channels, yielding a dispersive Lorentzian curve centred at zero-field for each output channel. The central linear portion of this curve is used for field discrimination.

3. MEG methods

MEG recordings of human subjects using two four-channel sensors were obtained inside a magnetically shielded room (MSR) at The Mind Research Network, Albuquerque, NM. The
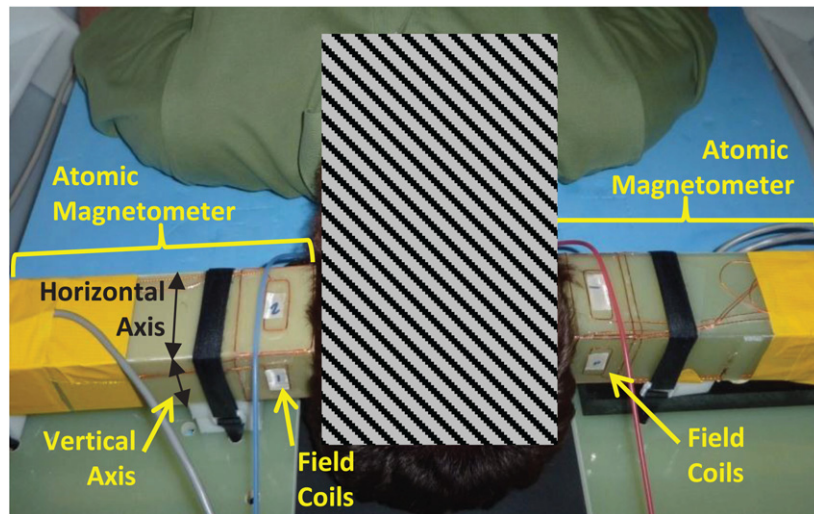
Figure 2. A human subject preparing for an auditory evoked response MEG recording. A four-channel SERF atomic magnetometer sensor is placed on each side of the head above the ear. Field zeroing and field modulation coils are integrated into each sensor, allowing the sensitive axis to be selected as either the horizontal or vertical direction.

sensors were mounted on opposite sides of the head above each ear to maximize the sensitivity to activity in the auditory cortex (see figure 2). Auditory tones at 1000 Hz and lasting 250 ms were presented in both ears at randomized times of either 900, 1000, or 1100 ms. The recorded brain responses from 330 stimuli were bandpass filtered from 2–55 Hz and combined to create a time-locked average. In our previous work with a single four-channel AM sensor (Johnson *et al* 2010), the auditory evoked response measured by the AM channels was shown to compare favourably with SQUID recordings of the auditory response. Therefore, no additional cross-validation studies were performed for this work.

The MSR provides a shielding factor of approximately 1000, leading to an environment of ∼100 nanotesla (nT) dc fields and gradients of ∼100 picotesla cm^{-1}. In order to operate the SERF AM in its linear regime, the ambient field at the sensor must be nulled to significantly less than the magnetic resonance width, ∼5 nT in our case. Therefore, additional field-zeroing capability is needed inside the MSR. In our previous single-sensor MEG work (Johnson *et al* 2010), a system of 18 coils wound on a cylinder large enough to accommodate the human subject was used to zero the ambient fields and provide field modulation. While this coil system has sufficient degrees of freedom to zero the field at multiple locations for multi-sensor operation, it cannot conveniently provide field modulations perpendicular to the optical axes of multiple sensors. We therefore integrated coils onto each sensor vacuum housing sufficient for both field zeroing and field modulation. The field is zeroed at the left hand sensor in figure 2 by applying constant currents to the large 18-coil system. Any remaining field at the right hand sensor is zeroed by applying constant currents to the coils wrapped on the right hand sensor. A well-documented zeroing procedure (Seltzer and Romalis 2004, Wyllie *et al* 2012a) is used to determine the required currents. Modulated fields at 1 kHz are applied to one of the two sets of coils perpendicular to the optical axis. The direction of the modulated field determines the sensitive axis of the magnetometer. We refer to the two possible sensitivity axes as 'horizontal' (parallel to the MSR floor) and 'vertical' (perpendicular to the MSR floor) as shown in figure 2.
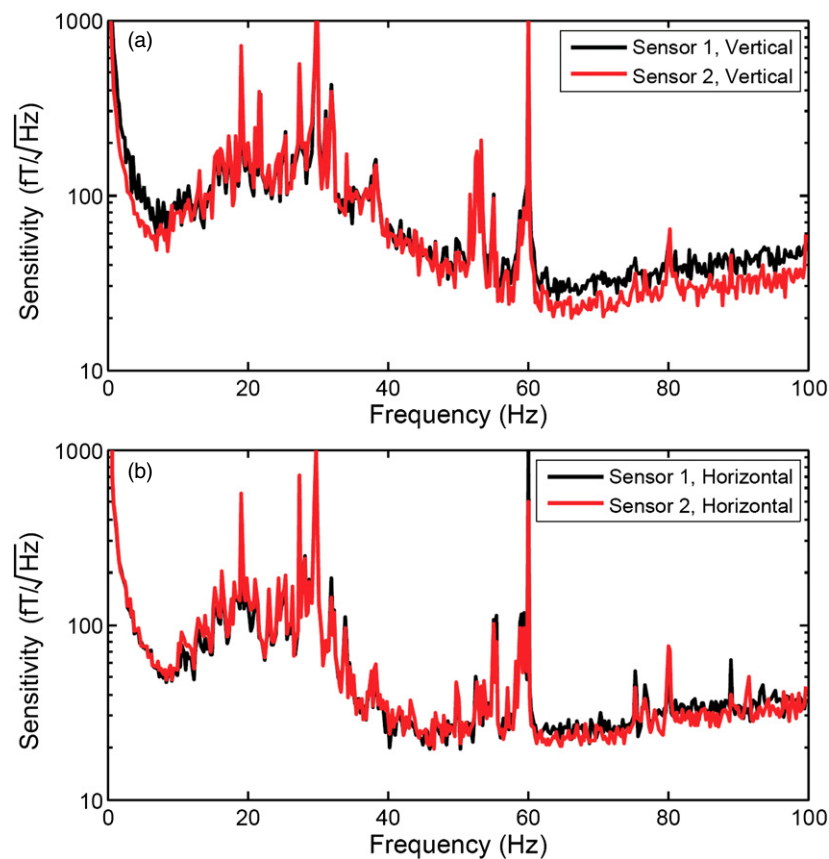
Figure 3. Magnetic noise measured inside the magnetically shielded room. Background noise was measured in the (a) vertical and (b) horizontal directions. Spectra were measured simultaneously with both sensors. The similarity in the noise spectra across sensors implies the presence of noise that is highly correlated between sensors.

The magnetic noise in the MSR was measured and is shown in figure 3. Ambient noise was measured by zeroing the ambient dc fields, turning on the appropriate modulated field, and recording the output signals on each magnetometer channel in the time domain. Noise spectra were subsequently obtained by taking the fast Fourier transform (FFT) of the sampled channels and multiplying the result by the experimentally determined signal-to-field conversion factor. Additionally, each spectrum in figure 3 is normalized to the bandwidth of the magnetometer by dividing the FFT by the measured frequency response of the device. Noise spectra were measured with all channels of both sensors, and using modulated fields along the vertical and horizontal axes. However, only the noise from a single channel of each sensor is shown in figure 3. The MSR noise is significantly higher than the ~ 5 fT/$\sqrt{\text{Hz}}$ intrinsic sensitivity of our device (Johnson *et al* 2010), with a noise level between 15–30 Hz of ~ 100 fT/$\sqrt{\text{Hz}}$. The background magnetic noise recorded by both sensors is nearly identical, indicating that the noise detected by one sensor is strongly correlated with the noise present at the other sensor.

The large magnetic noise level in the MSR makes it highly desirable to remove common-mode noise as effectively as possible. The noise spectra from the two sensors are very similar, implying uniform background magnetic noise that could in principle be removed from both sensors. One option for suppressing noise is to implement open-loop gradiometry

by subtracting the signals from adjacent channels on the same sensor. However, when the gradiometer baseline is much less than the distance to the biomagnetic source, most of the signal is also common-mode and the signal-to-noise of the gradiometric output is poor. This applies to our system where the baseline (i.e. the distance between adjacent channels) is only ~4 mm while the distance to the biomagnetic sources is several centimetres. As a result, our noise suppression efforts did not focus on this gradiometric method, although with minimal effort we did achieve noise suppression of ~15 dB. An alternative technique for generating gradiometric output is to operate a closed-loop feedback system wherein external fields are measured with a 'reference' sensor. The reference output is used to drive current in coils surrounding the other sensors that actively cancel the external fields. Closed-loop feedback systems using planar AM arrays for MCG have achieved 40 dB noise suppression in a first order gradiometer (Wyllie *et al* 2012a) and 30 dB suppression in a second-order gradiometer (Bison *et al* 2009). However, in our system both sensors detect biomagnetic fields, so a suitable reference sensor is unavailable. For these reasons, we seek an alternative to open-loop gradiometry or reference-sensor subtraction to isolate MEG signals from external interference.

In a multi-channel system, signal processing techniques offer an alternative strategy for improving the signal-to-noise ratio. Common techniques for isolating MEG signals from external magnetic interference, such as signal-space projection (SSP) (Uusitalo and Ilmoniemi 1997) and signal-space separation (Taulu *et al* 2004), represent signals from an N-sensor array as a vector in an *N* dimensional signal space. Relevant MEG signal vectors are significantly different than magnetic interference signal vectors, and the interfering signals can be removed via spatial filtering to increase the signal-to-noise ratio. Because the direction of the external interference vector is near-static, SSP is commonly implemented by measuring the signal vector in the absence of a human subject and removing signals parallel to this vector in subsequent MEG recordings. Because our sensors are not rigidly positioned and move when the subject's head is placed between the two magnetometers, data taken without the human subject in the system could not be utilized for SSP. In the data presented below, we perform SSP utilizing the signals measured in a time window when an evoked response is not expected. Specifically, we use data taken at least 400 ms after a stimulus has been presented but before the next stimulus presentation. We identify the vector in signal space most likely due to ambient magnetic field noise by finding the point in time at which the signal deviates maximally from the mean of the data in this time window. Once this vector is found, we project the data into a perpendicular space (Uusitalo and Ilmoniemi 1997). A new SSP vector is found after each presented stimulus in order to account for any drift in the external noise. Another signal processing technique, principal component analysis (PCA), identifies the vector in signal space parallel to the largest fluctuations on the magnetometer outputs. Assuming these fluctuations are due to correlated noise from external sources, removing all signals parallel to this direction will remove much of the correlated noise. The MEG recording data presented in section 4 take advantage of these signal analysis techniques to improve the signal-to-noise ratio.

4. MEG results

Our two-sensor MEG recordings have significant correlated noise between the two sensors, and the signal-to-noise ratio is sufficiently low that it is difficult to identify clear evoked responses on the raw data without resorting to low-pass filtering at <10 Hz. Because the noise is correlated, PCA or SSP can be used to increase the signal-to-noise ratio and enable detection of clear evoked responses without resorting to stringent low-pass filtering. The evoked response waveforms and signal-to-noise ratios resulting from SSP and PCA are similar, and only the SSP results are presented.
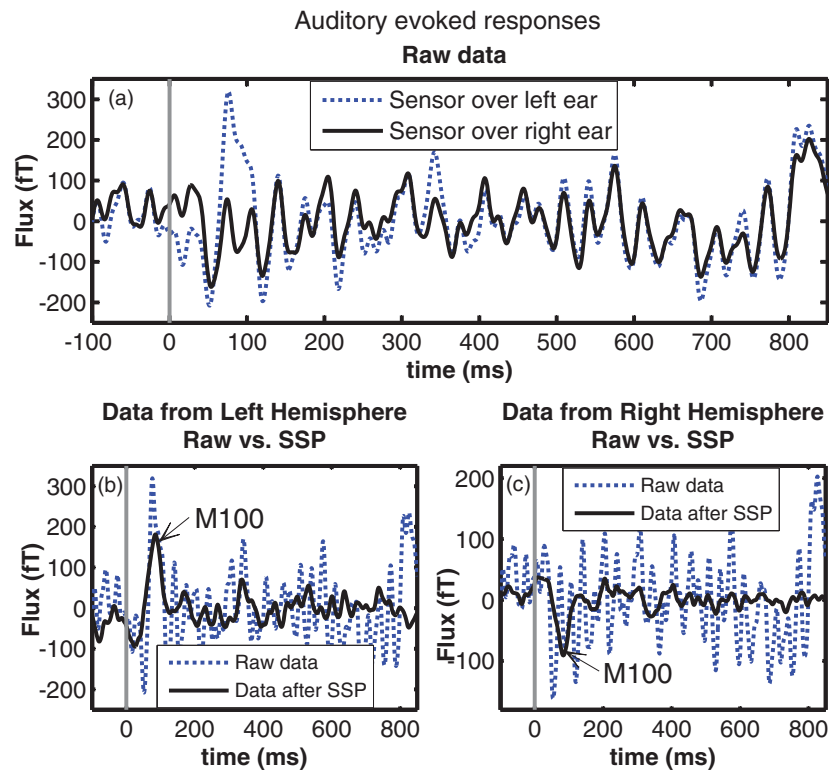
Figure 4. Auditory evoked responses recorded simultaneously with two sensors, one over each hemisphere. Displayed signals were measured along the vertical sensitivity axis, and only a single channel is displayed from each sensor. Each curve is an average of 330 1000-Hz auditory stimuli presented at $t = 0$, as indicated by the vertical line, and lasting 250 ms. Signals are bandpass filtered from 2–55 Hz. Significant correlated noise is visible on the raw data signals shown in (a). Signal-space projection removes most of the correlated noise, revealing clear M100 evoked responses that are detected by the sensor located over the left (b) and right (c) hemispheres.

Figure 4 shows the evoked responses measured in the vertical and horizontal directions from a single human subject. Auditory stimuli were presented in both ears as described in section 3, with one sensor placed on the scalp above the left ear and a second sensor placed on the scalp above the right ear. Each waveform is an average of 330 stimuli and has been bandpass filtered from 2–55 Hz. Only one channel from each sensor is displayed. Even after averaging hundreds of stimuli, the raw data magnetometer signals are dominated by correlated noise (see figure 4(a)). This noise is most likely produced by an external field that is nearly identical at each sensor, consistent with the noise spectrum measured in our shielded room (see figure 3). SSP is performed as discussed in section 3 in order to remove most of the correlated noise. The resulting signal-to-noise improvement is apparent in figures 4(b) and 4(c), where a clear M100 auditory evoked response is seen on the signal-space projected data approximately 90 ms after the presented stimuli, consistent with a typical M100 response (Hämäläinen *et al* 1993).

Figure 5 displays the auditory evoked responses from a human subject measured on all eight magnetometry channels, four from each sensor, and along both the vertical and horizontal sensitivity axes. The SSP, filtering, and number of averages are identical to those described in the previous paragraph. Because the signal space is small (two four-channel sensors), SSP
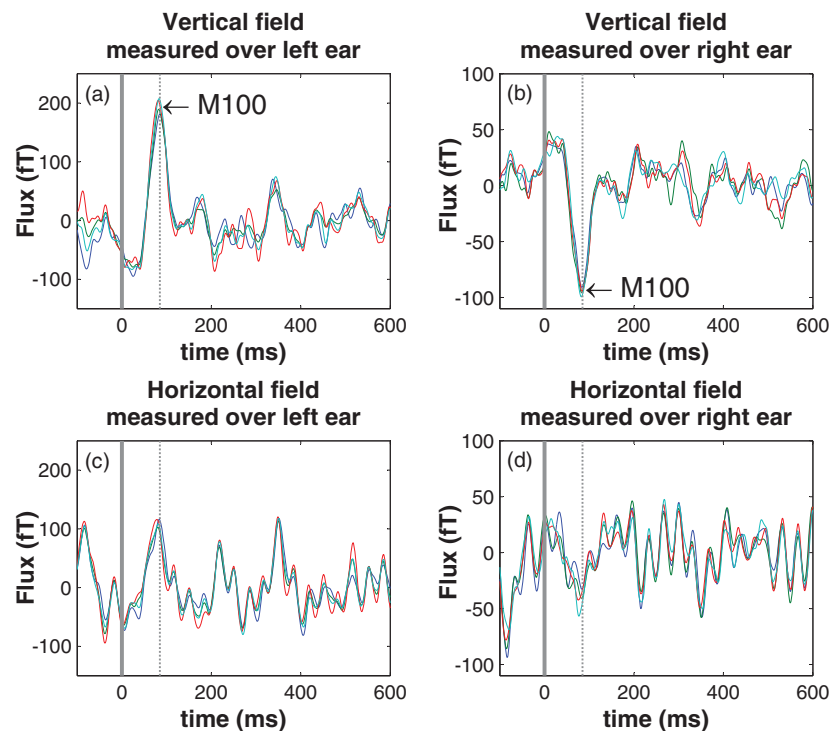
Figure 5. Auditory responses measured in both the vertical ((a) and (b)) and horizontal ((c) and (d)) directions. (a) and (c) were acquired with a four-channel sensor located over the left ear; (b) and (d) were acquired over the right ear. Each curve is an average of 330 1000-Hz auditory stimuli presented at time = 0, as indicated by the solid vertical line, and lasting 250 ms. Bandpass filtering from 2–55 Hz and signal-space projection has been performed. The M100 peak is clear along the vertical axis, as labelled in (a) and (b). There is a peak in the horizontal data that is correlated in time with the vertical M100 peak, as indicated by the dotted vertical lines. However, the signal-to-noise is too low to confidently identify a horizontal M100 peak, indicating that the sensor was placed such that the evoked field was primarily along the vertical direction.

removes not only correlated noise but also any evoked response signal parallel to the correlated noise in signal space. Signals remaining after SSP must therefore be predominantly caused by fields that are in opposite directions at the two sensors. When the vertical sensitivity axis is selected, clear M100 responses are present on all channels of the sensor over the left ear (figure 5(a)) and on all channels of the sensor over the right ear (figure 5(b)). When the horizontal sensitivity axis is selected, there appears to be a small peak that is correlated in time with the M100 peak seen on the vertical data, as indicated by the vertical dotted lines in figures 5(c) and 5(d), but the signal-to-noise ratio on this peak is insufficient to claim clear detection of an M100 peak. We conclude that our sensor placement resulted in the evoked response being primarily along the vertical sensitivity axis of each sensor. Also, note that we are detecting the responses with only two potentially poorly placed sensors. Our placement of each sensor was guided only by inference, and we would likely have better results with more coverage that would allow us to pick from the best responses.

Auditory evoked responses were obtained for three subjects, with the results shown in figure 6. The waveforms for each subject are detected along the vertical sensitivity axis and are the result of averaging 330 1000-Hz auditory responses that have been filtered with a 2–55 Hz bandpass filter and SSP. For each subject, a single data channel from each sensor is displayed.
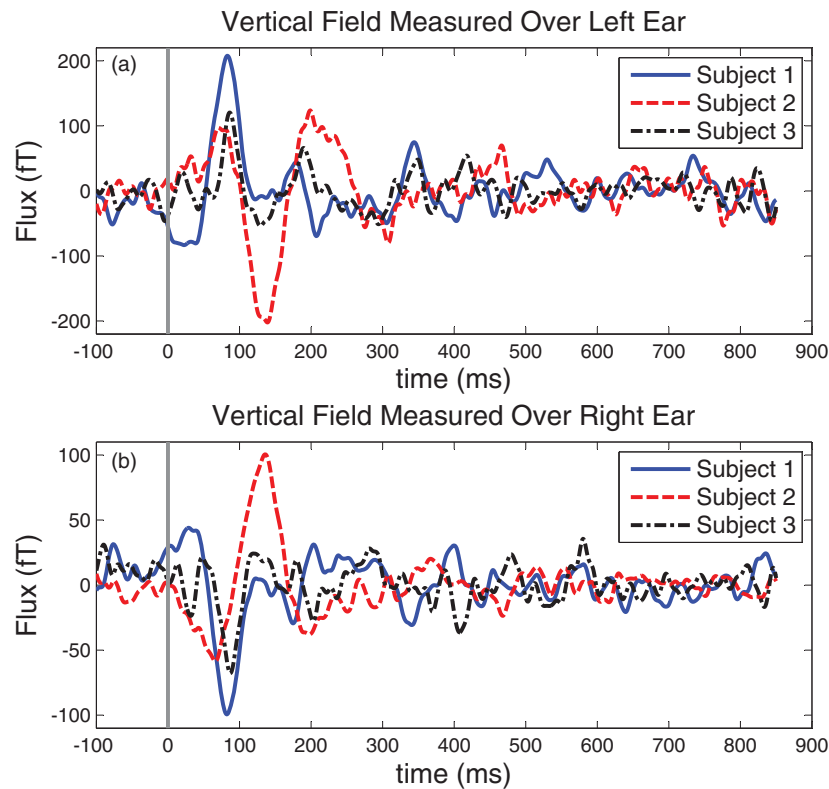
Figure 6. Auditory evoked responses recorded for three human subjects with sensors mounted over the (a) left and (b) right ears. The data from subject 1 is that which is presented in figures 4 and 5. Each curve is an average of 330 1000-Hz auditory stimuli presented at time = 0, as indicated by the vertical line, and lasting 250 ms. Bandpass filtering from 2–55 Hz and signal-space projection has been performed. Although the shape of the individual responses are different, for each subject the waveform detected over the left hemisphere appears to be highly correlated in time with the waveform detected over the right ear.

The shape of the waveforms varies considerably across individuals. However, for each subject the waveform detected over the left hemisphere (figure 6(a)) appears to be highly correlated in time with the waveform detected above the right hemisphere (figure 6(b)), indicating a consistently detected response on both sensors for each individual.

5. Conclusion

In conclusion, using two simultaneously operated fibre-coupled, multi-channel rubidium SERF magnetometer sensors, we have detected the magnetic field produced by the brain of multiple human subjects. The two sensors were placed on the scalp above the right and left ears near the location of the auditory cortex, and auditory evoked response MEG signals were recorded for multiple individuals. Signal processing techniques such as SSP, which can only be implemented in multi-channel systems, were used to greatly increase the signal-to-noise ratio of the evoked responses. We envision a future AM-based MEG system that extends our method by densely arraying similar sensors around the head. This work represents the first

demonstration of MEG signals detected with a multi-channel, multi-sensor AM system, and is a significant step toward the development of a future system for low-cost, non-cryogenic, whole-head MEG. As the next step toward this goal, we are actively redesigning the sensor to make it sufficiently small for dense packing around the head. In addition, we are investigating the optimal sensor array geometry in preparation for building an array with a sufficient number of sensors to perform magnetic source localization.

Acknowledgments

References

Allred J C, Lyman R N, Kornack T W and Romalis M V 2002 High-sensitivity atomic magnetometer unaffected by spin-exchange relaxation *Phys. Rev. Lett.* **89** 130801

Balabas M V, Karaulanov T, Ledbetter M P and Budker D 2010 Polarized alkali-metal vapor with minute-long transverse spin-relaxation time *Phys. Rev. Lett.* **105** 070801

Belfi J, Bevilacqua G, Biancalana V, Cartaleva S, Dancheva Y and Moi L 2007 Cesium coherent population trapping magnetometer for cardiosignal detection in an unshielded environment *J. Opt. Soc. Am.* B **24** 2357–62

Bison G, Castagna N, Hofer A, Knowles P, Schenker J L, Kasprzak M, Saudan H and Weis A 2009 A room temperature 19-channel magnetic field mapping device for cardiac signals *Appl. Phys. Lett.* **95** 173701

Bison G, Wynands R and Weis A 2003a Dynamical mapping of the human cardiomagnetic field with a room-temperature, laser-optical sensor *Opt. Express* **11** 904–9

Bison G, Wynands R and Weis A 2003b A laser-pumped magnetometer for the mapping of human cardiomagnetic fields *Appl. Phys.* B **76** 325–8

Dang H B, Maloof A C and Romalis M V 2010 Ultrahigh sensitivity magnetic field and magnetization measurements with an atomic magnetometer *Appl. Phys. Lett.* B **97** 151110

Fomin I, Sinelnikova S, Koslov A N, Uranov V and Gorshkov V 1983 On recording the heart's magnetic field *Kardiologija* **23** 66–68

Hämäläinen M, Hari R, Ilmoniemi R J, Knuutila J and Lounasmaa O V 1993 Magnetoencephalography—theory, instrumentation, and applications to noninvasive studies of the working human brain *Rev. Mod. Phys.* **65** 413–97

Happer W and Mathur B S 1967 Effective operator formalism in optical pumping *Phys. Rev.* **163** 12–25

Happer W and Tam A C 1977 Effect of rapid spin exchange on the magnetic-resonance spectrum of alkali vapors *Phys. Rev.* A **16** 1877–91

Happer W and Tang H 1973 Spin-exchange shift and narrowing of magnetic resonance lines in optically pumped alkali vapors *Phys. Rev. Lett.* **31** 273–6

Johnson C and Schwindt P D 2010 A two-color pump probe atomic magnetometer for magnetoencephalography *Proc. IEEE Int. Frequency Control Symp.* pp 371–5

Johnson C, Schwindt P D D and Weisend M 2010 Magnetoencephalography with a two-color pump-probe, fiber-coupled atomic magnetometer *Appl. Phys. Lett.* **97** 243703

Knappe S, Sander T H, Kosch O, Wiekhorst F, Kitching J and Trahms L 2010 Cross-validation of microfabricated atomic magnetometers with superconducting quantum interference devices for biomagnetic applications *Appl. Phys. Lett.* **97** 133703

Koch H 2004 Recent advances in magnetocardiography *J. Electrocardiol.* **37** 117–22

Kominis I K, Kornack T W, Allred J C and Romalis M V 2003 A subfemtotesla multichannel atomic magnetometer *Nature* **422** 596–9

Ledbetter M P, Savukov I M, Acosta V M, Budker D and Romalis M V 2008 Spin-exchange-relaxation-free magnetometry with Cs vapor *Phys. Rev.* A **77** 033408

Lima E A, Irimia A and Wikswo J P 2006 *The Magnetic Inverse Problem* 1st edn (Hoboken, NJ: Wiley) pp 139–267

Livanov M N, Koslov A N, Sinelnikova S E, Kholodov J A, Markin V P, Gorbach A M and Korinewsky A V 1981 Record of the human magnetocardiogram by the quantum gradiometer with optical pumping *Adv. Cardiol.* **28** 78–80

Sander T H, Preusser J, Mhaskar R, Kitching J, Trahms L and Knappe S 2012 Magnetoencephalography with a chip-scale atomic magnetometer *Biomed. Opt. Express* **3** 981–90

Schwindt P D D, Knappe S, Shah V, Hollberg L, Kitching J, Liew L A and Moreland J 2004 Chip-scale atomic magnetometer *Appl. Phys. Lett.* **85** 6409

Seltzer S J and Romalis M V 2004 Unshielded three-axis vector operation of a spin-exchange-relaxation-free atomic magnetometer *Appl. Phys. Lett.* **85** 4804–6

Sternickel K and Braginski A I 2006 Biomagnetism using SQUIDs: status and perspectives *Supercond. Sci. Technol.* **19** S160

Taulu S, Kajola M and Simola J 2004 Suppression of interference and artifacts by the signal space separation method *Brain Topogr.* **16** 269–75

Uusitalo M and Ilmoniemi R 1997 Signal-space projection method for separating MEG or EEG into components *Med. Biol. Eng. Comput.* **35** 135–40

Vrba J, Nenonen J and Trahms L 2006 *Biomagnetism* (Hoboken, NJ: Wiley) pp 269–389

Wyllie R, Kauer M, Smetana G S, Wakai R T and Walker T G 2012a Magnetocardiography with a modular spin-exchange relaxation-free atomic magnetometer array *Phys. Med. Biol.* **57** 2619–32

Wyllie R, Kauer M, Wakai R T and Walker T G 2012b Optical magnetometer array for fetal magnetocardiography *Opt. Lett.* **37** 2247–9

Xia H, Baranga A B A, Hoffman D and Romalis M V 2006 Magnetoencephalography with an atomic magnetometer *Appl. Phys. Lett.* **89** 211104